ACS APPLIED MATERIALS & INTERFACES

Research Article

Cite This: ACS Appl. Mater. Interfaces 2018, 10, 19218−19225

www.acsami.org

Enhanced Piezoelectric Response in Hybrid Lead Halide Perovskite Thin Films via Interfacing with Ferroelectric $PbZr_{0.2}Ti_{0.8}O_3$

Jingfeng Song,[†,∥] Zhiyong Xiao,[†,∥] Bo Chen,[‡] Spencer Prockish,[†] Xuegang Chen,[†] Anil Rajapitamahuni,[†] Le Zhang,[†] Jinsong Huang,[‡,§] and Xia Hong*[,†,§]

[†]Department of Physics and Astronomy, University of Nebraska-Lincoln, Lincoln, Nebraska 68588-0299, United States

[‡]Department of Mechanical and Materials Engineering, University of Nebraska-Lincoln, Lincoln, Nebraska 68588-0526, United States

[§]Nebraska Center for Materials and Nanoscience, University of Nebraska-Lincoln, Lincoln, Nebraska 68588-0298, United States

Supporting Information

ABSTRACT: We report a more than 10-fold enhancement of the piezoelectric coefficient d_{33} of polycrystalline $CH_3NH_3PbI_3$ ($MAPbI_3$) films when interfacing them with ferroelectric $PbZr_{0.2}Ti_{0.8}O_3$ (PZT). Piezoresponse force microscopy (PFM) studies reveal $d_{33}^{MAPbI_3}$ values of 0.3−0.4 pm/V for $MAPbI_3$ deposited on Au, indium tin oxide, and $SrTiO_3$ surfaces, with small phase angle fluctuating at length scales smaller than the grain size. In sharp contrast, on samples prepared on epitaxial PZT films, we observe large-scale polar domains exhibiting clear, close to 180° PFM phase contrasts, pointing to polar axes along the film normal. By separating the piezoresponse contributions from the $MAPbI_3$ and PZT layers, we extract a significantly higher $d_{33}^{MAPbI_3}$ of ∼4 pm/V, which is attributed to the enhanced alignment of the MA molecular dipoles promoted by the unbalanced surface potential of PZT. We also discuss the effect of the interfacial screening layer on the preferred polar direction.

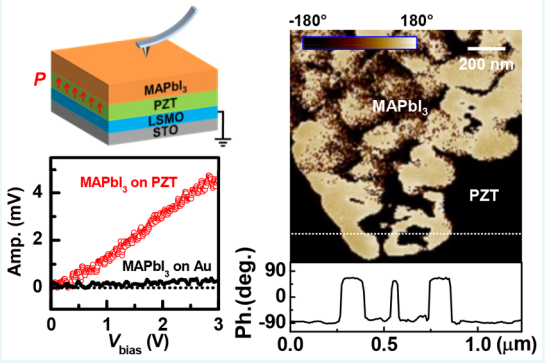

KEYWORDS: *hybrid perovskite, piezoelectricity, piezoresponse force microscopy, ferroelectrics, polar alignment*

INTRODUCTION

Organolead trihalide perovskites such as $CH_3NH_3PbI_3$ ($MAPbI_3$) have gained significant research interests in recent years because of their high power conversion efficiency,[1−4] strong solar absorption,[1,2] and long charge diffusion lengths,[5,6] making them promising for developing high-performance photovoltaic applications. It has been shown theoretically that these materials are polar,[7,8] which is corroborated by the experimental reports on piezoelectricity[9−13] and ferroelasticity[14,15] in $MAPbI_3$. The observations of photoinduced enhancement in the piezoelectric coefficient d_{33}[8,9] and the photostriction effect[16] further suggest a strong connection between the polar nature and their optical response. As the organic cations possess molecular dipoles that can rotate when subject to external stimuli such as an electric field,[4,17] a highly debated proposal to account for the high power conversion efficiency involves the existence of randomly oriented ferroelectric domains, where the internal field within the domain wall (DW) can promote the photocarrier separation and reduce recombination,[3,7,18] similar to the mechanism driving the high photovoltaic voltage in multiferroic $BiFeO_3$.[19,20] In previous studies, polar domains have been directly imaged in $MAPbI_3$ via piezoresponse force microscopy (PFM)[9,21−23] and second harmonic generation techniques,[24] and polarization switching hysteresis has also been reported.[22,24] Despite the extensive research carried out to probe ferroelectricity in $MAPbI_3$, the nature of the polarization and its role in the photovoltaic response are yet to be unambiguously identified.

Capitalizing on the piezoelectric properties, the application potential of the hybrid perovskites as piezoelectric generators or energy harvesting devices has also been explored.[12,13] For $MAPbI_3$ single crystals, a d_{33} value of 2.7 pm/V has been reported from direct optical measurement,[11] close to that of quartz (∼2.0 pm/V)[25] but much smaller than the values for other widely used piezoelectric materials such as ZnO (12 pm/V)[26] and $Pb(Zr,Ti)O_3$ (up to 400 pm/V).[27] Local d_{33} value of 6 pm/V was obtained via PFM in polycrystalline thin films,[9] whereas the average response of the sample over large scale can be compromised due to the disordered molecular dipoles. Despite the relatively small d_{33} value, $MAPbI_3$ has the notable advantages of low-cost production, light-weight, and being mechanically flexible and compatible with large-scale roll-to-roll manufacturing,[28,29] making it a highly viable material choice for large-scale flexible and wearable electronics that can be self-powered by simultaneous solar and mechanical energy harvesting.[30,31] It is thus of high technological interest to

Received: February 27, 2018
Accepted: May 7, 2018
Published: May 7, 2018

DOI: 10.1021/acsami.8b03403
ACS Appl. Mater. Interfaces 2018, 10, 19218−19225

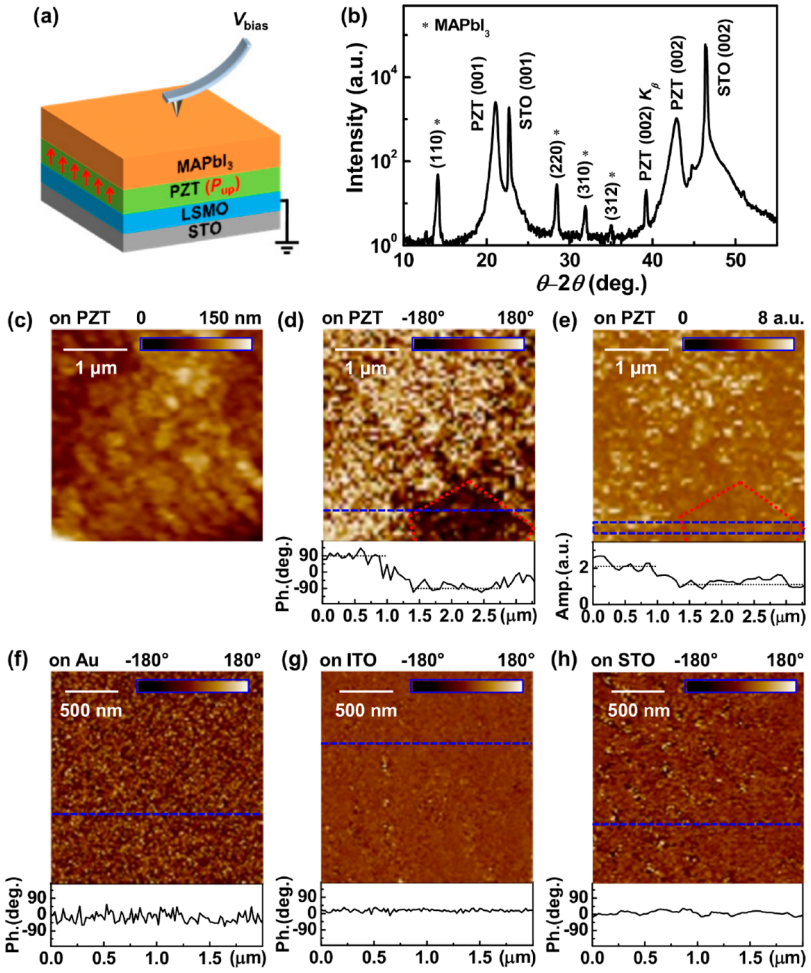

Figure 1. (a) Sample schematic. (b) X-ray scan and (c) AFM topography of a 300 nm $MAPbI_3$ film on PZT. (d) PFM phase and (e) amplitude images taken on the same sample area as in (c). The dotted lines serve as a guide to the eye. (f–h) PFM phase images taken on $MAPbI_3$ films on (f) Au, (g) ITO, and (h) STO base layers. The lower panels in (d–h) show the signal profiles along the dashed lines/box.

develop an effective material strategy to engineer the polar axis in this material for optimized piezoelectric response.

In this work, we report a more than 10-fold enhancement in the piezoelectric response of polycrystalline $MAPbI_3$ thin films when interfacing with an epitaxial ferroelectric $PbZr_{0.2}Ti_{0.8}O_3$ (PZT) layer. PFM studies showed that $MAPbI_3$ films prepared on Au, indium tin oxide (ITO), and $SrTiO_3$ (STO) surfaces exhibit net $d_{33}^{MAPbI_3}$ values of 0.3–0.4 pm/V, with small PFM phase angle fluctuation at length scales smaller than the sample grain size. In sharp contrast, films deposited on PZT exhibit large-scale domain structures with the polar axes along the film normal, with a significantly higher $d_{33}^{MAPbI_3}$ value of ∼4 pm/V obtained for both polarization up (P_{up}) and down (P_{down}) domains. Such an enhancement has been attributed to the surface potential of PZT induced by unbalanced surface charge, which promotes the alignment of the molecular dipoles of $MAPbI_3$ at the domain nucleation stage during sample annealing, while the preferred polar direction depends on the strength of interfacial screening.

EXPERIMENTAL SECTION

We deposited 20–300 nm $MAPbI_3$ films via spin-coating on four types of base layers, PZT, Au, ITO, and STO thin films, followed by thermal annealing at 100 °C.[32] The 50 nm PZT and STO films were deposited epitaxially on (001) STO substrates with a conducting buffer layer of 6–7 nm $La_{0.67}Sr_{0.33}MnO_3$ (LSMO), which serves as the bottom electrode (Figure 1a). The details of the sample deposition can be found in the Supporting Information. The as-grown PZT is uniformly polarized in the P_{up} state (see Figure S2 in the Supporting Information). To minimize moisture-induced sample degradation,[33] the $MAPbI_3$ films were prepared in a glovebox and sealed under an N_2 atmosphere immediately after deposition to be transferred to the characterization apparatus.

X-ray diffraction scans show that $MAPbI_3$ films on all four types of base layers are polycrystalline, with the highest intensity peaks corresponding to the (110) and (220) planes of the tetragonal phase (Figure 1b and Supporting Information). The extracted lattice constants agree well with the reported bulk values.[34] Atomic force microscopy (AFM) studies reveal relatively smooth surface morphology, with typical grain sizes of 200–400 nm and root-mean-square roughness of 6–20 nm (Figure 1c and Supporting Information). The AFM and PFM studies were carried out using a Bruker MultiMode 8 AFM system. The PFM measurements were taken in the contact, vertical mode, with an ac voltage V_{bias} applied to the conductive AFM tip and the bottom electrode grounded. The PFM signals obtained were based on the out-of-plane piezoresponse. We conducted PFM imaging close to the resonant frequency of the cantilever in contact (300 ± 20 kHz) with V_{bias} = 0.15 V and acquired the d_{33} values at 50 kHz, well below both the free-space resonance frequency (∼75 kHz) and the resonance of the cantilever with sample in contact. There is less than 20% variation in the PFM signal amplitude in the frequency range of 20–60 kHz, and we worked with 50 kHz to optimize the signal stability and signal-to-noise ratio (see detailed discussion in the

DOI: 10.1021/acsami.8b03403
ACS Appl. Mater. Interfaces 2018, 10, 19218–19225

Supporting Information). The high frequency employed helps eliminate the artifacts due to ionic electromigration within $MAPbI_3$.[35] All measurements were carried out in an N_2 atmosphere and within the same day of $MAPbI_3$ preparation.

RESULTS AND DISCUSSION

We first compared the PFM images taken on $MAPbI_3$ films deposited on different base layers (Figure 1d–h). For all samples, at V_{bias} = 0.15 V, the PFM signals of the same area are stable in sequential imaging, with no signs of domain switching. For films prepared on Au (Figure 1f), ITO (Figure 1g), and STO (Figure 1h) surfaces, the phase response fluctuates around 0° at the length scale of 50–100 nm. The length scale of the phase and amplitude fluctuation is much smaller than the typical grain size, and the spatial inhomogeneity of the signals within a grain cannot be correlated with the surface morphology (see Figures S8–S10 in the Supporting Information). Such fluctuations in the PFM response may originate from the variation of the polar axis within a crystalline grain, pointing to a relatively low DW energy.[36] This is consistent with the polar liquid scenario for the molecular dipole reorientations,[37] where the electrostatic and elastic energy of the DW can be minimized through dielectric screening and local polaron formation. On the 300 nm $MAPbI_3$ film deposited on PZT, on the other hand, the PFM image exhibits a qualitatively different phase landscape with much larger variation (Figure 1d). We observed over micron-size domain areas, where the phase angle is centered around either +90° or −90°, suggesting that the polar axes for both types of domains are normal to the film surface and opposite to each other. Superimposed on the large-scale domains is a mosaic phase structure with characteristic length scales on the order of about 100 nm. Similar signal variation is also observed in the amplitude image (Figure 1e), even though not all short length-scale structures can be recognized, likely due to the lower spatial resolution for the amplitude signal on the soft sample surface. Given the relatively smooth surface morphology in this area (Figure 1c), the 180° phase change cannot be due to the artifacts associated with sharp step edges or sample pinholes.

The emergence of large-scale P_{up} and P_{down} domains is more evident in thinner samples (20–60 nm) on PZT. In Figure 2a–c, we imaged a 25 ± 5 nm thick sample close to the film boundary, where we can monitor the PFM responses of $MAPbI_3$ and bare PZT at the same time. Besides the PFM signal variation that can be well-correlated with the grain boundaries, as shown in the topography image (Figure 2a), the domains coexisting in the same grain also show distinct amplitude responses (Figure 2c), ruling out possible artifacts due to grain boundaries or sharp step edges. In addition to the mosaic phase variation similar to those observed on the thick films, there exists large-scale domains exhibiting clean, uniform signals close to ±90°, with many of the domains extending over several grains (Figure 2b). The bare PZT region, on the other hand, shows homogenous phase angle of −90° and amplitude response, corresponding to the as-grown P_{up} state (Figures 2d and S2 in the Supporting Information). As a control experiment, we also imaged the P_{down} and P_{up} domains written on bare PZT (Figure 2d). The PFM phase response of the ±90° domains in $MAPbI_3$ (Figure 2b) bears strong resemblance to that of the P_{up}–P_{down} domain structure in PZT. In addition, the region with phase angle in phase with that of PZT exhibits significantly higher amplitude signal than the

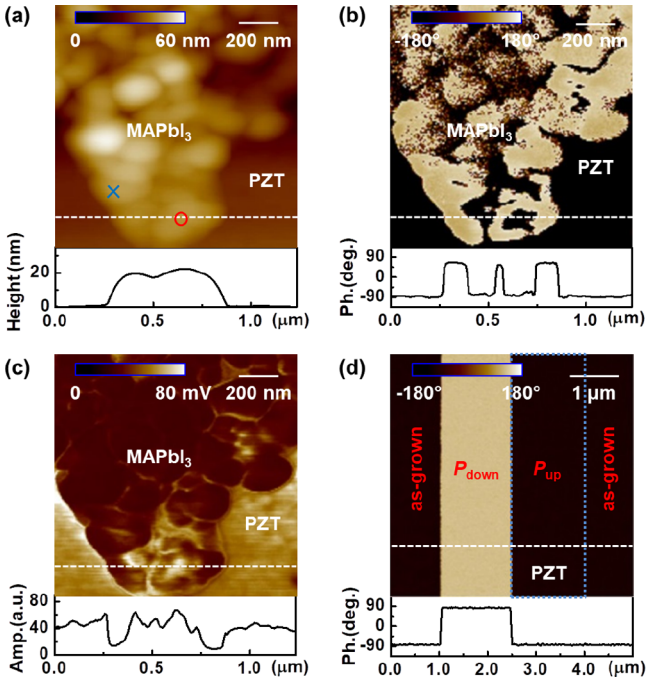

Figure 2. (a) AFM topography, (b) PFM phase, and (c) amplitude images taken on a 25 ± 5 nm $MAPbI_3$ film on PZT. The lower panels show the signal profiles along the dashed lines. (d) PFM phase image of P_{down} and P_{up} domains written on bare PZT. The P_{up} domain (outlined with a dotted box) cannot be differentiated from the as-grown state.

region that is out of phase with PZT polarization (Figure 2c). Such a difference is due to the relative alignment between the polar axes of $MAPbI_3$ and PZT, which can result in either constructive or destructive PFM responses. As the PFM imaging voltage (V_{bias} = 0.15 V) is insufficient to switch the polarization of PZT underneath, the spontaneous domain formation and PFM amplitude variation can only be intrinsic to $MAPbI_3$. For the smaller mosaic structures observed in Figures 1d and 2b, the phase fluctuation amplitude also well-exceeds the noise floor of the phase signal (<5°). We thus conclude that these fluctuations are real rather than due to imaging noise. This is more evident in the upper half region in Figure 2b, where both mosaic domain patterns and large-scale domains were imaged in the same line scan. Given the characteristic length scale of these mosaic domains are approaching the image resolution, we cannot differentiate whether the relatively small phase angle variation (i.e., <90°) is originating from the change of underlying polar alignment or a result of imaging limitation for small-scale 180° domains, where the signal contrast is not well-resolved.

We then carried out quantitative PFM amplitude analysis, collecting the amplitude signal A at a lower frequency (20–50 kHz) while ramping V_{bias} from 0 to 3 V at 0.1 V/s (Figure 3a). We kept V_{bias} to be lower than the coercive voltage of the PZT layer (Figure S2 in the Supporting Information) to ensure that the polarization of PZT remains to be in the as-grown state (uniform P_{up}) during the voltage sweep. We focused on a spot showing +90° phase angle (marked with a blue cross in Figure 2a) and one that shows a −90° phase response (red circle). Both spots reside at the central area of a grain so that we can exclude extrinsic effects due to grain boundary-induced ion migration, pinholes, sharp height variation, or strain gradient.[38,39] On both sites, $A(V_{bias})$ exhibits a quasi-linear

DOI: 10.1021/acsami.8b03403
ACS Appl. Mater. Interfaces 2018, 10, 19218–19225

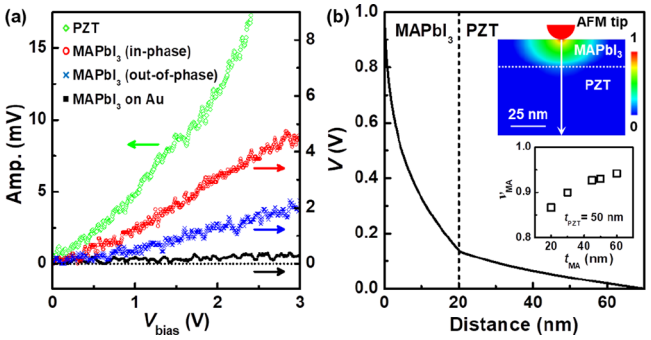

Figure 3. (a) PFM amplitude vs V_{bias} measured on bare PZT, two spots marked in Figure 2a, and the data taken on a 25 nm $MAPbI_3$ film on Au. (b) Simulated voltage vs distance from the AFM tip across 20 nm $MAPbI_3$/50 nm PZT at V_{bias} = 1 V. The dashed line highlights the $MAPbI_3$/PZT interface. Insets: simulated cross-sectional potential distribution (upper) and ν_{MA} vs t_{MA} (lower).

behavior (Figure 3a). Similar quasi-linear V_{bias}-dependence of the piezoresponse has been observed in all $MAPbI_3$ samples prepared on different surfaces, with no sign of switching the polar direction. At V_{bias} = 3 V, the amplitude responses of these two spots reach 2 and 4 mV, respectively. For comparison, we also showed the data taken on a 25 nm film prepared on Au, whose amplitude signal only reaches ~0.28 mV at V_{bias} = 3 V, similar to the samples on ITO and STO (see Figures S8–S10 in the Supporting Information). For bare PZT, the amplitude exceeds 4 mV at V_{bias} = 1 V.

To calculate d_{33}, we converted the amplitude A into the sample displacement $u_{tot} = AS/I$, where S = 50 pm/V is the tip sensitivity and I = 16 is the vertical gain, and extracted $d_{33} = \partial u_{tot}/\partial V_{bias}$ from the initial slope of $A(V_{bias})$. A superlinear dependence emerges at V_{bias} > 2 V, which can be attributed to a quadratic contribution of the ferroelastic effect.[40] For bare PZT, we obtained a d_{33}^{PZT} value of 19 ± 1 pm/V, comparable with the reported values for PZT films with similar composition using optical method.[41] PFM measurements taken on the P_{up} and P_{down} domains written on PZT also reveal similar d_{33} values, further proving that the as-grown PZT is fully polarized in a monodomain state (see Figure S6b in the Supporting Information).

For the $MAPbI_3$ films, we obtained a d_{33} value of about 0.3 pm/V for the samples on Au, similar to those on ITO (Figures S8 and S9 in the Supporting Information). To extract d_{33} for the films on PZT and STO, we performed finite element analysis to calculate the voltage distribution across the $MAPbI_3$ and PZT (STO) layers.[42] Figure 3b (upper inset) shows the simulated potential distribution through a heterostructure with 20 nm $MAPbI_3$ and 50 nm PZT at V_{bias} = 1 V, assuming a point contact with the AFM tip and a global ground provided by the LSMO layer. For modeling, we used the dielectric constants of 100 for PZT[43] and 32 for $MAPbI_3$.[6] For our sample geometry, the majority of the bias voltage is always applied through the $MAPbI_3$ layer (Figure 3b), with the fractional voltage ($\nu_{MA} = V_{MAPbI_3}/V_{bias}$) changing from 87 to 93% as the $MAPbI_3$ film thickness t_{MA} increases from 20 to 60 nm (Figure 3b lower inset). The absence of the superlinear behavior in $A(V_{bias})$ for $MAPbI_3$ also confirms that the voltage fraction across PZT ($\nu_{PZT} = V_{PZT}/V_{bias}$) is small. On the basis of the simulated voltage distribution, we calculated the d_{33} value of $MAPbI_3$ using

$$\frac{\partial u_{tot}}{\partial V_{bias}} = d_{33}^{MAPbI_3}\nu_{MA} \pm d_{33}^{PZT}\nu_{PZT} \quad (1)$$

where we used d_{33}^{PZT} = 19 pm/V for PZT, "+" for constructive (in-phase), and "−" for destructive (out-of-phase) piezoelectric responses between these two layers. For the sample shown in Figure 2, we extracted $d_{33}^{MAPbI_3}$ = 3.7 ± 0.1 pm/V for the P_{up} region and 4.2 ± 0.2 pm/V for the P_{down} region. Similar modeling was performed to deduce $d_{33}^{MAPbI_3}$ for films prepared on STO (Figure S10d in the Supporting Information).

Figure 4a summarizes the d_{33} values for $MAPbI_3$ samples on different base layers. For the 20–60 nm films on PZT, d_{33} varies from 3.3 to 4.2 pm/V, with no apparent dependence on the polar direction. This result is comparable with the single-crystal value[11] and 1 order of magnitude higher than the films on Au, ITO, and STO (0.3–0.4 pm/V). The optimal amplitude response, in conjunction with the ±90° phase angle of the piezoelectric response, collectively points to fully aligned polar domains in the $MAPbI_3$ films on PZT. The small, highly fluctuating phase angles observed in the samples on Au, ITO, and STO (Figure 1f–h), on the other hand, are consistent with a random, isotropic distribution of the polar axes, which would yield a small net piezoelectric response.

For the films on PZT, the evolution from large-scale domains (Figure 2b,c) in the 20–60 nm films to a mosaic domain structure (Figure 1d,e) observed in the 300 nm film further suggests that the interaction between $MAPbI_3$ and PZT is an interfacial rather than bulk effect. In canonical ferroelectrics, it is known that domain formation is a result of the energy competition among the long-range dipole–dipole interaction, short-range elastic energy, and various disorder potentials.[44] We first consider the possible contribution of lattice strain, which has been shown to lead to spontaneous domain formation in polycrystalline $MAPbI_3$.[14,21] Despite the variation of surface morphology, the $MAPbI_3$ films prepared on different types of base layers exhibit similar crystalline structures (Figure 1b and Supporting Information), consistent with previous reports on polycrystalline $MAPbI_3$ films grown on substrates with different surface conditions.[45,46] The extracted lattice parameters for all types of samples are comparable and in excellent agreement with the bulk lattice constants in the tetragonal phase (Table S1 in Supporting Information), which suggests an insignificant variation in the strain states among these samples. In addition, the observed polar domain structures are mostly with irregular shape and size, isolated, and have no direct correlation with either the sample morphology or the polycrystalline grain distribution (Figures 1 and 2), whereas those features would have strong influences on the strain distribution. These characteristics of the polar domain structure are in sharp contrast to those reported in refs 14 and 21, where the internal strain has resulted in highly regular stripe domains that conform well with the grain structure. We thus rule out strain as the driving mechanism for the polar domain and enhanced piezoresponse in films on PZT.

We then consider the contribution of the electrostatic energy. A possible mechanism is that the surface potential of PZT due to the high-density bound charge promotes the alignment of the polar axis in the initial domain nucleation stage. Once the domains with P_{up} and P_{down} states are seeded at the interface, it is energetically unfavorable for the growth of domains with other polar axis because of the long-range dipole–dipole interaction, an important energy scale in

DOI: 10.1021/acsami.8b03403
ACS Appl. Mater. Interfaces 2018, 10, 19218–19225

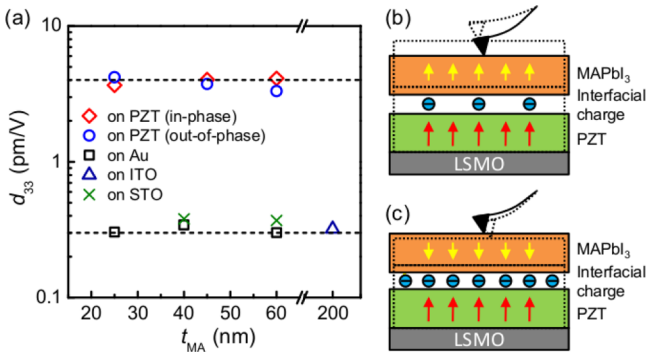

Figure 4. (a) d_{33} vs t_{MA} for $MAPbI_3$ on PZT, Au, ITO, and STO. The dashed lines serve as the guide to the eye. (b,c) Schematics for the constructive (b) and destructive (c) piezoelectric responses between $MAPbI_3$ and PZT, with the underscreening and overscreening interfacial charge layers, respectively.

ferroelectric materials that competes with the elastic energy and disorder potential in determining the DW energy and domain structures.[36,47,48] For example, enhanced piezoelectric response has been achieved in the ferroelectric copolymer poly(vinylidene-fluoride-trifluorethylene) [P(VDF-TrFE)] by optimizing the local dipole alignment through precise microstructure control.[49] A similar scenario has also been adopted to explain the enhanced open voltage and photovoltaic efficiency in $BiFeO_3$ when interfaced with $MAPbI_3$.[20]

The fact that the samples deposited on all four types of bases layers have similar crystal structures yields strong evidence that the enhanced piezoresponse in the samples on PZT is decoupled from the bulk crystalline symmetry. We thus propose that such an enhancement may originate from the promoted alignment of the A-site MA molecular dipole, which induces local polaronic lattice distortion. This kind of local distortion has been observed experimentally in $MAPbI_3$,[50] and the molecular reorientations when subject to an external electric field have been attributed to a liquid-type short-range polar interaction.[37] Unlike the perovskite oxide ferroelectrics, where the ferroelectric instability is directly associated with the displacement of ions at different lattice sites, for example, the B-site cations and the oxygens at the tetragonal face center positions, the dipole moment of $MAPbI_3$ originates from the A-site MA molecules.[4,16] Because of the extremely localized nature of these dipoles, the elastic energy associated with the lattice distortion, which competes with the dipole−dipole interaction to promote the in-plane alignment of the dipoles, is much weaker than the ferroelectric oxide. As a result, there is a significantly lower energy penalty in decoupling the local dipole orientation from the bulk crystal structure. It has been shown both theoretically[7,8] and experimentally[51] that the MA dipole can rotate under external electrical or optical excitations. Although the reorientation of the MA molecule can induce dynamic local structural distortion in $MAPbI_3$, as confirmed by simulations[7,52] and high-energy-resolution inelastic X-ray scattering studies,[50] no signature of the structural symmetry breaking has been detected by the Bragg diffraction technique.[50] A likely scenario is that when the molecular dipoles are not fully rotated out of plane, their in-plane components remain to be disordered, preventing a long-range order that can alter the crystal structure. This model naturally explains why the domain structure in $MAPbI_3$ cannot be correlated with the polycrystalline grains, and the corresponding d_{33} values are comparable with that of bulk single crystals regardless of different grain crystal orientations.[11] As the polar alignment is induced by the surface potential of PZT, we expect that the effect would diminish when the interfacial $MAPbI_3$ layer provides sufficient screening, either through thermal carriers or dielectric screening, to fully compensate this potential. Our study showed similar $d_{33}^{MAPbI_3}$ values (Figure 4a) and polar domain distributions in 25−60 nm $MAPbI_3$ thin films (Figure 2 and Supporting Information), whereas the characteristic domain size for the 300 nm film is notably smaller (Figure 1d,e), signaling a larger fraction of the MA dipoles with enhanced in-plane component with increasing distance from the interface. This thickness dependence is in reasonable agreement with the depletion widths of 45−160 nm reported in thick polycrystalline $MAPbI_3$ films.[53,54]

The dipole field interaction alone, however, cannot explain why a predominant fraction of the domains has the polar axis antialigned with the polarization of PZT. What has not been taken into account is the existence of a charge screening layer at the $MAPBI_3$/PZT interface that can change the polarity of PZT surface potential. It is known that the ferroelectric surface can attract charged adsorbates and water molecules from the ambient to screen the surface bound charge.[55] We propose that it is the unbalanced fraction of the surface potential that affects the polar alignment of the MA dipoles during the crystallization of $MAPbI_3$. Depending on whether the screening strength is underscreening or overscreening, the preferred polar axis of $MAPbI_3$ would be either parallel (Figure 4b) or antiparallel (Figure 4c) to that of PZT, respectively. In our experiments, the $MAPbI_3$ layers were prepared on the PZT surface in ambient at room temperature, with the polarization close to be fully screened prior to deposition. The samples were then annealed at 100 °C for forming polyscrystalline films, while PZT polarization decreases due to the pyroelectric effect. The existing screening layer would then lead to an overscreening to the high-temperature polarization. As the screening adsorbate layer is trapped at the $MAPbI_3$ and PZT interface, its exchange with the ambient charge can be a relatively slow process. In the meantime, the majority of the sample surface possesses unbalanced surface charge, which is screened through the reorientation of the MA dipoles, aligned antiparallel with PZT polarization. To further examine the feasibility of this scenario, we performed in situ Kelvin probe force microscopy (KPFM) measurements to probe the surface potential of the domain structures on PZT with varying temperatures. As discussed in the Supporting Information (Figure S11), the surface potential difference between the P_{up} and P_{down} domains diminishes with time in ambient and indeed reverses sign when the sample is heated at 100 °C, yielding strong support to the proposed model for the antialigned domains. Such a polarity change of unbalanced surface potential has been previously observed on ferroelectric $BaTiO_3$[56] and PZT[57] thin films via variable temperature KPFM measurements. The thermally induced unbalanced surface screening charge has also been probed in ferroelectric-gated graphene transistors, where the switching hysteresis in graphene can evolve from being in phase to out of phase with the ferroelectric gate switching with increasing temperature.[58−60] The coexistence of both polar domains, on the other hand, may be due to the stochastic nature of surface charge absorption, which requires the precise knowledge of the surface condition of PZT. This scenario also suggests that it is possible to engineer the polar axis of polycrystalline $MAPbI_3$

DOI: 10.1021/acsami.8b03403
ACS Appl. Mater. Interfaces 2018, 10, 19218−19225

thin films in a uniform state by controlling the surface screening condition of the ferroelectric base layer.

CONCLUSIONS

In summary, working with $MAPbI_3$/PZT heterostructures, we have shown that the presence of an interface polarization can promote the polar alignment in polycrystalline $MAPbI_3$ thin films, leading to a net piezoelectric response comparable with that of bulk single crystals. We expect that the similar effect can be achieved by exploiting the out-of-plane polarization of other ferroelectric base layers, such as $BaTiO_3$ and PVDF. Interfacing with the polymeric ferroelectrics is particularly promising for developing large-scale flexible/wearable electronics. Our work also suggests that the local dipole orientation can be decoupled from the bulk crystalline orientation, a property that is in sharp contrast to the conventional oxide ferroelectrics, yielding strong support to a polar liquid scenario of the reorientation of the local MA dipole.[37,51] The demonstrated synergy between the polar properties of the hybrid perovskite and an interfacial ferroelectric material can be utilized to engineer the polar alignment in $MAPbI_3$. For example, it is possible to impose different domain structures in $MAPbI_3$ by preparing it on ferroelectrics with prewritten domains, providing a controlled route to studying the relation between the photoresponse of the sample and the DW density. Our study thus points to an effective material strategy for advancing our fundamental understanding of the role of the polar properties in the high conversion efficiency of the hybrid perovskite, as well as facilitating the development of organolead trihalide perovskite thin film-based flexible electronics with integrated electronic, mechanical, and photovoltaic functionalities.

ASSOCIATED CONTENT

Supporting Information

The Supporting Information is available free of charge on the ACS Publications website at DOI: 10.1021/acsami.8b03403.

Preparation and characterization of $MAPbI_3$, PZT, and STO thin films; details of the PFM measurements; PFM characterizations of 45 and 60 nm $MAPbI_3$ thin films on PZT; PFM characterizations of $MAPbI_3$ thin films on Au, ITO, and STO; and KPFM measurements of PZT (PDF)

AUTHOR INFORMATION

Corresponding Author

*E-mail: xia.hong@unl.edu.

ORCID

Jingfeng Song: 0000-0002-3463-0196
Zhiyong Xiao: 0000-0003-2461-2338
Jinsong Huang: 0000-0002-0509-8778
Xia Hong: 0000-0002-7873-5774

Author Contributions

‖J.S. and Z.X. contributed equally to this work. X.H. conceived and supervised the project. B.C. and J.H. prepared the $MAPbI_3$ films. X.C. prepared the PZT thin films. A.R. prepared the STO thin films. X.C. and L.Z. carried out the structural characterizations. J.S., Z.X., and S.P. carried out the scanning probe studies, finite element analysis, and data modeling. J.S. and X.H. wrote the manuscript. All authors discussed the results and contributed to the manuscript preparation.

Funding

This work was supported by the NSF Nebraska Materials Research Science and Engineering Center (MRSEC) grant no. DMR-1420645 (sample preparation), NSF grant no. DMR-1409622 (oxide thin film deposition), NSF Career grant no. DMR-1148783 (structural characterization), and NSF grant no. OIA-1538893 (scanning probe studies and manuscript preparation). S.P. acknowledges support from Nebraska Public Power District through the Nebraska Center for Energy Sciences Research. The research was performed in part in the Nebraska Nanoscale Facility: National Nanotechnology Coordinated Infrastructure and the Nebraska Center for Materials and Nanoscience, which are supported by the National Science Foundation under Award ECCS: 1542182, and the Nebraska Research Initiative.

Notes

The authors declare no competing financial interest.

ACKNOWLEDGMENTS

The authors would like to thank Sergei Kalinin, Angus Kingon, and Nitin P. Padture for insightful discussions and Dong Wang and Kong Liu for experimental assistance.

ABBREVIATIONS

$MAPbI_3$, methylammonium lead halides; PZT, lead zirconate titanate; STO, strontium titanate; LSMO, lanthanum strontium manganite; ITO, indium tin oxide; AFM, atomic force microscopy; PFM, piezo-response force microscopy; KPFM, Kelvin probe force microscopy; P(VDF-TrFE), poly(vinylidene fluoride-trifluoroethylene).

REFERENCES

(1) Kojima, A.; Teshima, K.; Shirai, Y.; Miyasaka, T. Organometal Halide Perovskites as Visible-Light Sensitizers for Photovoltaic Cells. *J. Am. Chem. Soc.* **2009**, *131*, 6050−6051.

(2) Green, M. A.; Ho-Baillie, A.; Snaith, H. J. The emergence of perovskite solar cells. *Nat. Photonics* **2014**, *8*, 506−514.

(3) Hsiao, Y.-C.; Wu, T.; Li, M.; Liu, Q.; Qin, W.; Hu, B. Fundamental physics behind high-efficiency organo-metal halide perovskite solar cells. *J. Mater. Chem. A* **2015**, *3*, 15372−15385.

(4) Berry, J.; Buonassisi, T.; Egger, D. A.; Hodes, G.; Kronik, L.; Loo, Y.-L.; Lubomirsky, I.; Marder, S. R.; Mastai, Y.; Miller, J. S.; Mitzi, D. B.; Paz, Y.; Rappe, A. M.; Riess, I.; Rybtchinski, B.; Stafsudd, O.; Stevanovic, V.; Toney, M. F.; Zitoun, D.; Kahn, A.; Ginley, D.; Cahen, D. Hybrid Organic-Inorganic Perovskites (HOIPs): Opportunities and Challenges. *Adv. Mater.* **2015**, *27*, 5102−5112.

(5) Shi, D.; Adinolfi, V.; Comin, R.; Yuan, M.; Alarousu, E.; Buin, A.; Chen, Y.; Hoogland, S.; Rothenberger, A.; Katsiev, K.; Losovyj, Y.; Zhang, X.; Dowben, P. A.; Mohammed, O. F.; Sargent, E. H.; Bakr, O. M. Low trap-state density and long carrier diffusion in organolead trihalide perovskite single crystals. *Science* **2015**, *347*, 519−522.

(6) Dong, Q.; Fang, Y.; Shao, Y.; Mulligan, P.; Qiu, J.; Cao, L.; Huang, J. Electron-hole diffusion lengths > 175 mu m in solution-grown $CH_3NH_3PbI_3$ single crystals. *Science* **2015**, *347*, 967−970.

(7) Frost, J. M.; Butler, K. T.; Brivio, F.; Hendon, C. H.; van Schilfgaarde, M.; Walsh, A. Atomistic Origins of High-Performance in Hybrid Halide Perovskite Solar Cells. *Nano Lett.* **2014**, *14*, 2584−2590.

(8) Liu, S.; Zheng, F.; Grinberg, I.; Rappe, A. M. Photoferroelectric and Photopiezoelectric Properties of Organometal Halide Perovskites. *J. Phys. Chem. Lett.* **2016**, *7*, 1460−1465.

(9) Coll, M.; Gomez, A.; Mas-Marza, E.; Almora, O.; Garcia-Belmonte, G.; Campoy-Quiles, M.; Bisquert, J. Polarization Switching and Light-Enhanced Piezoelectricity in Lead Halide Perovskites. *J. Phys. Chem. Lett.* **2015**, *6*, 1408−1413.

DOI: 10.1021/acsami.8b03403
ACS Appl. Mater. Interfaces 2018, 10, 19218−19225

(10) Seol, D.; Han, G. S.; Bae, C.; Shin, H.; Jung, H. S.; Kim, Y. Screening effect on photovoltaic performance in ferroelectric CH3NH3PbI3 perovskite thin films. *J. Mater. Chem. A* **2015**, *3*, 20352−20358.
(11) Dong, Q.; Song, J.; Fang, Y.; Shao, Y.; Ducharme, S.; Huang, J. Lateral-Structure Single-Crystal Hybrid Perovskite Solar Cells via Piezoelectric Poling. *Adv. Mater.* **2016**, *28*, 2816−2821.
(12) Ding, R.; Liu, H.; Zhang, X.; Xiao, J.; Kishor, R.; Sun, H.; Zhu, B.; Chen, G.; Gao, F.; Feng, X.; Chen, J.; Chen, X.; Sun, X.; Zheng, Y. Flexible Piezoelectric Nanocomposite Generators Based on Formamidinium Lead Halide Perovskite Nanoparticles. *Adv. Funct. Mater.* **2016**, *26*, 7708−7716.
(13) Kim, Y.-J.; Dang, T.-V.; Choi, H.-J.; Park, B.-J.; Eom, J.-H.; Song, H.-A.; Seol, D.; Kim, Y.; Shin, S.-H.; Nah, J.; Yoon, S.-G. Piezoelectric properties of CH3NH3PbI3 perovskite thin films and their applications in piezoelectric generators. *J. Mater. Chem. A* **2016**, *4*, 756−763.
(14) Hermes, I. M.; Bretschneider, S. A.; Bergmann, V. W.; Li, D.; Klasen, A.; Mars, J.; Tremel, W.; Laquai, F.; Butt, H.-J.; Mezger, M.; Berger, R.; Rodriguez, B. J.; Weber, S. A. L. Ferroelastic Fingerprints in Methylammonium Lead Iodide Perovskite. *J. Phys. Chem. C* **2016**, *120*, 5724−5731.
(15) Strelcov, E.; Dong, Q.; Li, T.; Chae, J.; Shao, Y.; Deng, Y.; Gruverman, A.; Huang, J.; Centrone, A. $CH_3NH_3PbI_3$ Perovskites: Ferroelasticity Revealed. *Sci. Adv.* **2017**, *3*, No. e1602165.
(16) Zhou, Y.; You, L.; Wang, S.; Ku, Z.; Fan, H.; Schmidt, D.; Rusydi, A.; Chang, L.; Wang, L.; Ren, P.; Chen, L.; Yuan, G.; Chen, L.; Wang, J. Giant photostriction in organic-inorganic lead halide perovskites. *Nat. Commun.* **2016**, *7*, 11193.
(17) Knop, O.; Wasylishen, R. E.; White, M. A.; Cameron, T. S.; Van Oort, M. J. M. Alkylammonium lead halides. Part 2. $CH_3NH_3PbX_3$ (X=Cl, Br, I) perovskites: cuboctahedral halide cages with isotropic cation reorientation. *Can. J. Chem.* **1990**, *68*, 412−422.
(18) Liu, S.; Zheng, F.; Koocher, N. Z.; Takenaka, H.; Wang, F.; Rappe, A. M. Ferroelectric Domain Wall Induced Band Gap Reduction and Charge Separation in Organometal Halide Perovskites. *J. Phys. Chem. Lett.* **2015**, *6*, 693−699.
(19) Yang, S. Y.; Seidel, J.; Byrnes, S. J.; Shafer, P.; Yang, C.-H.; Rossell, M. D.; Yu, P.; Chu, Y.-H.; Scott, J. F.; Ager, J. W.; Martin, L. W.; Ramesh, R. Above-bandgap voltages from ferroelectric photovoltaic devices. *Nat. Nanotechnol.* **2010**, *5*, 143−147.
(20) Zhao, P.; Bian, L.; Wang, L.; Xu, J.; Chang, A. Enhanced open voltage of $BiFeO_3$ polycrystalline film by surface modification of organolead halide perovskite. *Appl. Phys. Lett.* **2014**, *105*, 013901.
(21) Röhm, H.; Leonhard, T.; Hoffmann, M. J.; Colsmann, A. Ferroelectric domains in methylammonium lead iodide perovskite thin-films. *Energy Environ. Sci.* **2017**, *10*, 950−955.
(22) Fan, Z.; Xiao, J.; Sun, K.; Chen, L.; Hu, Y.; Ouyang, J.; Ong, K. P.; Zeng, K.; Wang, J. Ferroelectricity of CH3NH3PbI3 Perovskite. *J. Phys. Chem. Lett.* **2015**, *6*, 1155−1161.
(23) Kutes, Y.; Ye, L.; Zhou, Y.; Pang, S.; Huey, B. D.; Padture, N. P. Direct Observation of Ferroelectric Domains in Solution-Processed $CH_3NH_3PbI_3$ Perovskite Thin Films. *J. Phys. Chem. Lett.* **2014**, *5*, 3335−3339.
(24) Rakita, Y.; Bar-Elli, O.; Meirzadeh, E.; Kaslasi, H.; Peleg, Y.; Hodes, G.; Lubomirsky, I.; Oron, D.; Ehre, D.; Cahen, D. Tetragonal CH3NH3PbI3 is ferroelectric. *Proc. Natl. Acad. Sci. U.S.A.* **2017**, *114*, E5504−E5512.
(25) Zhang, S.; Yu, F. Piezoelectric Materials for High Temperature Sensors. *J. Am. Ceram. Soc.* **2011**, *94*, 3153−3170.
(26) Zhao, M.-H.; Wang, Z.-L.; Mao, S. X. Piezoelectric characterization of individual zinc oxide nanobelt probed by piezoresponse force microscope. *Nano Lett.* **2004**, *4*, 587−590.
(27) Haertling, G. H. Ferroelectric ceramics: History and technology. *J. Am. Ceram. Soc.* **1999**, *82*, 797−818.
(28) Hwang, K.; Jung, Y.-S.; Heo, Y.-J.; Scholes, F. H.; Watkins, S. E.; Subbiah, J.; Jones, D. J.; Kim, D.-Y.; Vak, D. Toward Large Scale Roll-to-Roll Production of Fully Printed Perovskite Solar Cells. *Adv. Mater.* **2015**, *27*, 1241−1247.
(29) Li, Y.; Meng, L.; Yang, Y.; Xu, G.; Hong, Z.; Chen, Q.; You, J.; Li, G.; Yang, Y.; Li, Y. High-efficiency robust perovskite solar cells on ultrathin flexible substrates. *Nat. Commun.* **2016**, *7*, 10214.
(30) Wen, Z.; Yeh, M.-H.; Guo, H.; Wang, J.; Zi, Y.; Xu, W.; Deng, J.; Zhu, L.; Wang, X.; Hu, C.; Zhu, L.; Sun, X.; Wang, Z. L. Self-powered textile for wearable electronics by hybridizing fiber-shaped nanogenerators, solar cells, and supercapacitors. *Sci. Adv.* **2016**, *2*, No. e1600097.
(31) Chen, J.; Huang, Y.; Zhang, N.; Zou, H.; Liu, R.; Tao, C.; Fan, X.; Wang, Z. L. Micro-cable structured textile for simultaneously harvesting solar and mechanical energy. *Nat. Energy* **2016**, *1*, 16138.
(32) Xiao, Z.; Dong, Q.; Bi, C.; Shao, Y.; Yuan, Y.; Huang, J. Solvent Annealing of Perovskite-Induced Crystal Growth for Photovoltaic-Device Efficiency Enhancement. *Adv. Mater.* **2014**, *26*, 6503−6509.
(33) Berhe, T. A.; Su, W.-N.; Chen, C.-H.; Pan, C.-J.; Cheng, J.-H.; Chen, H.-M.; Tsai, M.-C.; Chen, L.-Y.; Dubale, A. A.; Hwang, B.-J. Organometal halide perovskite solar cells: degradation and stability. *Energy Environ. Sci.* **2016**, *9*, 323−356.
(34) Baikie, T.; Fang, Y.; Kadro, J. M.; Schreyer, M.; Wei, F.; Mhaisalkar, S. G.; Graetzel, M.; White, T. J. Synthesis and crystal chemistry of the hybrid perovskite $(CH_3NH_3)PbI_3$ for solid-state sensitised solar cell applications. *J. Mater. Chem. A* **2013**, *1*, 5628−5641.
(35) Yuan, Y.; Wang, Q.; Shao, Y.; Lu, H.; Li, T.; Gruverman, A.; Huang, J. Electric-Field-Driven Reversible Conversion Between Methylammonium Lead Triiodide Perovskites and Lead Iodide at Elevated Temperatures. *Adv. Energy Mater.* **2016**, *6*, 1501803.
(36) Xiao, Z.; Hamblin, J.; Poddar, S.; Ducharme, S.; Paruch, P.; Hong, X. Effect of thermal annealing on ferroelectric domain structures in poly(vinylidene-fluoride-trifluorethylene) Langmuir-Blodgett thin films. *J. Appl. Phys.* **2014**, *116*, 066819.
(37) Zhu, H.; Miyata, K.; Fu, Y.; Wang, J.; Joshi, P. P.; Niesner, D.; Williams, K. W.; Jin, S.; Zhu, X.-Y. Screening in crystalline liquids protects energetic carriers in hybrid perovskites. *Science* **2016**, *353*, 1409−1413.
(38) Jesse, S.; Guo, S.; Kumar, A.; Rodriguez, B. J.; Proksch, R.; Kalinin, S. V. Resolution theory, and static and frequency-dependent cross-talk in piezoresponse force microscopy. *Nanotechnology* **2010**, *21*, 405703.
(39) Shao, Y.; Fang, Y.; Li, T.; Wang, Q.; Dong, Q.; Deng, Y.; Yuan, Y.; Wei, H.; Wang, M. Y.; Gruverman, A.; Shielda, J.; Huang, J. S. Grain boundary dominated ion migration in polycrystalline organic-inorganic halide perovskite films. *Energy Environ. Sci.* **2016**, *9*, 1752−1759.
(40) Li, S.; Cao, W.; Cross, L. E. The extrinsic nature of nonlinear behavior observed in lead zirconate titanate ferroelectric ceramic. *J. Appl. Phys.* **1991**, *69*, 7219−7224.
(41) Huang, Z.; Zhang, Q.; Corkovic, S.; Dorey, R.; Whatmore, R. Comparative measurements of piezoelectric coefficient of PZT films by Berlincourt, interferometer, and vibrometer methods. *IEEE Trans. Ultrason. Ferroelectrics Freq. Contr.* **2006**, *53*, 2287−2293.
(42) Song, J.; Lu, H.; Foreman, K.; Li, S.; Tan, L.; Adenwalla, S.; Gruverman, A.; Ducharme, S. Ferroelectric polymer nanopillar arrays on flexible substrates by reverse nanoimprint lithography. *J. Mater. Chem. C* **2016**, *4*, 5914−5921.
(43) Hong, X.; Posadas, A.; Zou, K.; Ahn, C. H.; Zhu, J. High-Mobility Few-Layer Graphene Field Effect Transistors Fabricated on Epitaxial Ferroelectric Gate Oxides. *Phys. Rev. Lett.* **2009**, *102*, 136808.
(44) Paruch, P.; Giamarchi, T.; Triscone, J.-M. Domain Wall Roughness in Epitaxial Ferroelectric $PbZr_{0.2}Ti_{0.8}O_3$ Thin Films. *Phys. Rev. Lett.* **2005**, *94*, 197601.
(45) Zhou, Y.; Game, O. S.; Pang, S.; Padture, N. P. Microstructures of Organometal Trihalide Perovskites for Solar Cells: Their Evolution from Solutions and Characterization. *J. Phys. Chem. Lett.* **2015**, *6*, 4827−4839.
(46) Bi, C.; Wang, Q.; Shao, Y.; Yuan, Y.; Xiao, Z.; Huang, J. Non-wetting surface-driven high-aspect-ratio crystalline grain growth for efficient hybrid perovskite solar cells. *Nat. Commun.* **2015**, *6*, 7747.

DOI: 10.1021/acsami.8b03403
ACS Appl. Mater. Interfaces 2018, 10, 19218−19225

(47) Paruch, P.; Kolton, A. B.; Hong, X.; Ahn, C. H.; Giamarchi, T. Thermal quench effects on ferroelectric domain walls. *Phys. Rev. B* **2012**, *85*, 214115.
(48) Xiao, Z.; Poddar, S.; Ducharme, S.; Hong, X. Domain wall roughness and creep in nanoscale crystalline ferroelectric polymers. *Appl. Phys. Lett.* **2013**, *103*, 112903.
(49) Choi, Y.-Y.; Sharma, P.; Phatak, C.; Gosztola, D. J.; Liu, Y. Y.; Lee, J.; Lee, B.; Li, J.; Gruverman, A.; Ducharme, S.; Hong, S. Enhancement of Local Piezoresponse in Polymer Ferroelectrics via Nanoscale Control of Microstructure. *ACS Nano* **2015**, *9*, 1809−1819.
(50) Beecher, A. N.; Semonin, O. E.; Skelton, J. M.; Frost, J. M.; Terban, M. W.; Zhai, H.; Alatas, A.; Owen, J. S.; Walsh, A.; Billinge, S. J. L. Direct Observation of Dynamic Symmetry Breaking above Room Temperature in Methylammonium Lead Iodide Perovskite. *ACS Energy Lett.* **2016**, *1*, 880−887.
(51) Selig, O.; Sadhanala, A.; Müller, C.; Lovrincic, R.; Chen, Z.; Rezus, Y. L. A.; Frost, J. M.; Jansen, T. L. C.; Bakulin, A. A. Organic Cation Rotation and Immobilization in Pure and Mixed Methylammonium Lead-Halide Perovskites. *J. Am. Chem. Soc.* **2017**, *139*, 4068−4074.
(52) Whalley, L. D.; Frost, J. M.; Jung, Y.-K.; Walsh, A. Perspective: Theory and simulation of hybrid halide perovskites. *J. Chem. Phys.* **2017**, *146*, 220901.
(53) Dymshits, A.; Henning, A.; Segev, G.; Rosenwaks, Y.; Etgar, L. The electronic structure of metal oxide/organo metal halide perovskite junctions in perovskite based solar cells. *Sci. Rep.* **2015**, *5*, 8704.
(54) Laban, W. A.; Etgar, L. Depleted hole conductor-free lead halide iodide heterojunction solar cells. *Energy Environ. Sci.* **2013**, *6*, 3249−3253.
(55) Kalinin, S. V.; Bonnell, D. A. Local potential and polarization screening on ferroelectric surfaces. *Phys. Rev. B: Condens. Matter Mater. Phys.* **2001**, *63*, 125411.
(56) Kalinin, S. V.; Johnson, C. Y.; Bonnell, D. A. Domain polarity and temperature induced potential inversion on the $BaTiO_3$ (100) surface. *J. Appl. Phys.* **2002**, *91*, 3816−3823.
(57) Segura, J. J.; Domingo, N.; Fraxedas, J.; Verdaguer, A. Surface screening of written ferroelectric domains in ambient conditions. *J. Appl. Phys.* **2013**, *113*, 187213.
(58) Hong, X. Emerging ferroelectric transistors with nanoscale channel materials: the possibilities, the limitations. *J. Phys.: Condens. Matter* **2016**, *28*, 103003.
(59) Rajapitamahuni, A.; Hoffman, J.; Ahn, C. H.; Hong, X. Examining Graphene Field Effect Sensors for Ferroelectric Thin Film Studies. *Nano Lett.* **2013**, *13*, 4374−4379.
(60) Yusuf, M. H.; Nielsen, B.; Dawber, M.; Du, X. Extrinsic and Intrinsic Charge Trapping at the Graphene/Ferroelectric Interface. *Nano Lett.* **2014**, *14*, 5437−5444.

DOI: 10.1021/acsami.8b03403
ACS Appl. Mater. Interfaces 2018, 10, 19218−19225